AGU PUBLICATIONS

JGR

Journal of Geophysical Research: Space Physics

RESEARCH ARTICLE

10.1002/2017JA023967

Special Section:

Observations, Simulations, and Theory of Electric Currents in the Solar System

Key Points:

- The latitude of the substorm onset is colocated with the interface between the R1 and R2 systems
- Both Region 1 (R1) and Region 2 (R2) current densities enhance at substorm onset
- Upward current density decreases prior to onset in a localized area, consistent with auroral dimming

Correspondence to:

J. C. Coxon,
work@johncoxon.co.uk

Citation:

Coxon, J. C., I. J. Rae, C. Forsyth, C. M. Jackman, R. C. Fear, and B. J. Anderson (2017), Birkeland currents during substorms: Statistical evidence for intensification of Regions 1 and 2 currents after onset and a localized signature of auroral dimming, *J. Geophys. Res. Space Physics*, *122*, 6455–6468, doi:10.1002/2017JA023967.

Received 30 JAN 2017
Accepted 13 JUN 2017
Accepted article online 16 JUN 2017
Published online 28 JUN 2017

Birkeland currents during substorms: Statistical evidence for intensification of Regions 1 and 2 currents after onset and a localized signature of auroral dimming

John C. Coxon[1], **I. Jonathan Rae**[2], **Colin Forsyth**[2], **Caitriona M. Jackman**[1], **Robert C. Fear**[1], **and Brian J. Anderson**[3]

[1]Department of Physics and Astronomy, University of Southampton, Southampton, UK, [2]Mullard Space Science Laboratory, University College London, Dorking, UK, [3]The John Hopkins University Applied Physics Laboratory, Laurel, Maryland, USA

Abstract We conduct a superposed epoch analysis of Birkeland current densities from AMPERE (Active Magnetosphere and Planetary Electrodynamics Response Experiment) using isolated substorm expansion phase onsets identified by an independently derived data set. In order to evaluate whether R1 and R2 currents contribute to the substorm current wedge, we rotate global maps of Birkeland currents into a common coordinate system centered on the magnetic local time of substorm onset. When the latitude of substorm is taken into account, it is clear that both R1 and R2 current systems play a role in substorm onset, contrary to previous studies which found that R2 current did not contribute. The latitude of substorm onset is colocated with the interface between R1 and R2 currents, allowing us to infer that R1 current closes just tailward and R2 current closes just earthward of the associated current disruption in the tail. AMPERE is the first data set to give near-instantaneous measurements of Birkeland current across the whole polar cap, and this study addresses apparent discrepancies in previous studies which have used AMPERE to examine the morphology of the substorm current wedge. Finally, we present evidence for an extremely localized reduction in current density immediately prior to substorm onset, and we interpret this as the first statistical signature of auroral dimming in Birkeland current.

1. Introduction

The canon on the relationship between substorms and field-aligned currents (also called Birkeland currents) started over a century ago. *Birkeland* [1908] described events which he called “polar elementary storms” and concluded that these storms must be caused by field-aligned currents near the auroral zone; this description was the first physical description of the substorm. Over 50 years later, *Akasofu* [1964] used a network of auroral imagers to identify two discrete phases of the substorm: the expansion phase (so called because of a brightening in the aurora and subsequent rapid motion toward the geomagnetic pole) and the recovery phase. *Akasofu* [1964] also defined the quiet phase as the period between the end of one recovery phase and the beginning of the next expansion phase. It was later understood that this phenomenon required a buildup of magnetic flux and energy, and so *McPherron* [1970] used ground magnetometer observations to define the growth phase as the missing phase of what he called the magnetospheric substorm.

The growth phase of the substorm is characterized by the interplanetary magnetic field (IMF) interconnecting with Earth’s magnetic field, resulting in the opening of flux and storage of energy in the magnetosphere. The expansion phase is dominated by nightside reconnection closing these field lines, and the recovery phase is the return of the system to quiescence. These three cycles repeat in a cycle of solar wind-magnetosphere coupling [*Dungey*, 1961], driving convection of plasma in the magnetosphere, which is coupled to the ionosphere by Birkeland currents [*Birkeland*, 1908, 1913]. As field lines are opened and closed, the polar cap expands and contracts [*Siscoe and Huang*, 1985; *Cowley and Lockwood*, 1992], referred to as the expanding/contracting polar cap (ECPC) paradigm [*Lockwood and Cowley*, 1992; *Milan et al.*, 2007]; the Birkeland current ovals move sympathetically, and previous studies have shown that the R1 current oval lies within 1° latitude of the open/closed field line boundary [*Clausen et al.*, 2013a].

Magnetic perturbations were observed by *Zmuda et al.* [1966] which were later found by *Cummings and Dessler* [1967] to be Birkeland currents. The global morphology of the currents was deduced by *Iijima and Potemra* [1976, 1978], who described two regions of Birkeland current representing distinct currents into and out of the ionosphere. The poleward region of current was defined as Region 1 (R1), closing via the magnetopause; the equatorward region was defined as Region 2 (R2), closing in the partial ring current on the nightside of Earth. At more active times, the R1 and R2 current systems lie farther equatorward than during more quiescent times, which can be explained in the context of the ECPC paradigm [*Clausen et al.*, 2012]. Birkeland currents are observed to be stronger during periods of enhanced magnetic reconnection at the dayside magnetopause and, consequently, during southward IMF [e.g., *Weimer*, 2001; *Anderson et al.*, 2014; *Coxon et al.*, 2014a, 2014b; *Carter et al.*, 2016]. The amount of Birkeland current flowing is dependent not only on magnetic reconnection but also on season and local time sector, due to ionospheric conductance, which varies seasonally and diurnally [*Fujii and Iijima*, 1987]. However, the Northern Hemisphere appears to experience more current flow than the Southern Hemisphere even when accounting for variations in ionospheric conductance [*Coxon et al.*, 2016].

Usually, Birkeland currents flowing into the ionosphere are closed through Pedersen currents, which then connect to Birkeland currents flowing out of the ionosphere, closing the system [e.g., *Hoffman et al.*, 1994; *Cowley*, 2000]. However, the magnetospheric current system is drastically changed by a substorm. A current disruption in the magnetotail causes current to be diverted along the magnetic field (as Birkeland currents) into the ionosphere, leading to an additional system known as the substorm current wedge (SCW) [*Clauer and McPherron*, 1974], in which there is some current disruption in the magnetotail which leads to a current flowing toward the ionosphere on the dawnside and away from the ionosphere on the duskside of the reconnection site in the magnetotail. The Birkeland currents diverted from the magnetotail in this manner are closed in the ionosphere by a substorm electrojet traditionally identified by the *AL* index [e.g., *Boström*, 1964; *Davis and Sugiura*, 1966, and references therein]. This picture has been supplemented by more detailed theories as to the nature of the currents flowing; more recent models of the SCW propose that it involves R1 and R2 currents, as current flows both toward and away from the ionosphere on both sides of the polar cap [*Birn et al.*, 1999; *Birn and Hesse*, 2014; *Sergeev et al.*, 2011, 2014a], and some observations have also been made which appear to show Region 0 (R0) current flowing poleward of the R1 current during substorms [*Fujii et al.*, 1994; *Hoffman et al.*, 1994; *Gjerloev and Hoffman*, 2002]. Observations of far more intricate structure have been made by Cluster, whereby tens of thin current sheets were observed, consistent with the traditional SCW when integrated over large spatial scales [*Forsyth et al.*, 2014a]. Observations of the Birkeland currents differ on the composition of the SCW. A recent principal component analysis of Birkeland currents showed no sign of a principal variability associated with substorms [*Milan et al.*, 2015], but most authors have observed some signature, whether it was the two-loop system [*Coxon et al.*, 2014b; *Sergeev et al.*, 2014a, 2014b] or only the traditional SCW [*Clausen et al.*, 2013a]. The DP-1 current system (the ionospheric signature of the substorm current wedge) was identified in a empirical orthogonal function analysis of SuperMAG data [*Shore et al.*, 2017]. For a more complete review of research into the substorm current wedge, we refer the reader to *Kepko et al.* [2015].

It has been confirmed that the Birkeland currents expand and contract in the same sense as the polar cap [*Clausen et al.*, 2012; *Carter et al.*, 2016]. *Coxon et al.* [2014b] observed that the current magnitudes of R1 and R2 (integrated over the whole of the polar cap) both slowly increased toward substorm expansion phase onset. Alongside this observation indicating that currents increase in a global sense, *Murphy et al.* [2012] observed a localized reduction in upward current density immediately prior to auroral substorm onset which they interpreted as evidence for a change in magnetosphere-ionosphere coupling, as upward field-aligned currents are colocated with the aurora both spatially and temporally [*Boström*, 1966; *Murphy et al.*, 2012, 2013; *Carter et al.*, 2016]. *Pellinen and Heikkila* [1978] presented ground-based observations of aurora near substorm onset in which they observed a reduction in auroral brightness 8–5 min before onset, and *Murphy et al.* [2012] interpreted their result as the signature of auroral dimming in the Birkeland current system.

It should be noted that there is some debate as to whether the substorm current wedge comprises R1/R2 currents; if the R1/R2 system is defined by currents closing via the magnetopause/partial ring current, then the SCW does not comprise R1/R2 currents because it maps to a disruption in the magnetotail. If, however, R1/R2 currents are simply defined by the sense of their ionospheric footprints, then the SCW can be well described in terms of R1/R2 currents. We adopt the latter definition and describe the SCW using R1 and R2 currents, after the example of some of the earliest work on this topic [*Iijima and Potemra*, 1978].

In this paper, therefore, we examine the role of the R1 and R2 current systems during substorms. We determine that both the R1 and R2 current systems contribute to the substorm current wedge [e.g., *Coxon et al.*, 2014b], rather than solely the R1 current system [e.g., *Clausen et al.*, 2013a]. We also examine the Birkeland currents in the coordinates close to substorm onset to determine that there is evidence for a highly localized reduction in current density immediately prior to substorm onset, which is consistent with previous observations of aurora and currents [*Pellinen and Heikkila*, 1978; *Murphy et al.*, 2012].

2. Data

2.1. AMPERE

The properties of the Birkeland currents can be inferred from the Active Magnetosphere and Planetary Electrodynamics Response Experiment (AMPERE) [*Anderson et al.*, 2000, 2014; *Waters et al.*, 2001]. AMPERE gives the radial current density in altitude-adjusted geomagnetic coordinates (AACGM) at an altitude of 780 km on a grid of 1° colatitude by 1 h magnetic local time (MLT). The data are computed over a 10 min sliding window, which is approximately the interspacecraft separation but which is evaluated every 2 min. Hence, each new 2 min evaluation contains new data and features in the data are visible on timescales below 10 min as a result of this approach [e.g., *Clausen et al.*, 2013a]. Therefore, the cadence is arguably better than 10 min but definitely not as good as 2 min. If we adopt time steps of 6 min, over half the data contributing to the evaluation is different between each time step. As such, we adopt 6 min time steps in this study, to show the evolution of the current densities. This choice also facilitates easy comparison with the plots of *Clausen et al.* [2013a]. We will use maps which AMPERE employs spherical cap harmonics to infer the current density across the polar cap from the magnetometers aboard the member satellites of the Iridium constellation, comprising 66 satellites in six orbital planes. A review of the work which has been done with the constellation is given by *Coxon et al.* [2017].

2.2. SOPHIE

We employ a recent technique, called SOPHIE (Substorm Onsets and Phases from H-Indices of the Electrojet), to independently determine substorm expansion phase onsets [*Forsyth et al.*, 2015]. The SOPHIE algorithm uses the time differential of the SuperMAG indices *SML* and *SMU* [*Newell and Gjerloev*, 2011], which can be considered equivalent to the *AL* and *AU* indices, to identify the onsets of expansion phases, recovery phases, and possible growth phases from 1996 to 2014 at a cadence of 1 min. The expansion phase is identified by times when the rate of change in *SML* is negative and is below some percentile threshold in the data. In this study, the 75% threshold is used, as recommended by *Forsyth et al.* [2015]: For a detailed discussion of how the expansion phase onsets identified by SOPHIE compare with other substorm lists, we refer the reader to the paper. We only use expansion phase onsets which are preceded in the SOPHIE data set by a growth phase; in this way, we filter out substorms which occur soon after another substorm, reducing the variability in the events analyzed.

SOPHIE does not identify the location of onset, so we use the colatitude and MLT of the magnetometer contributing to the *SML* index at each expansion phase onset time, in the same manner as the SuperMAG substorm list [*Newell and Gjerloev*, 2011]. SOPHIE does, however, provide a flag for phase identifications which occur when *SMU* and *SML* are of similar values [*Forsyth et al.*, 2015]. *Kamide and Kokubun* [1996] showed that the electrojets in the ionosphere are a combination of two factors: first, directly driven enhancements in ionospheric convection (due to magnetic reconnection) causing enhancements in the electrojets on the dawn and dusk flanks of the polar cap and second, the unloading of energy from the magnetotail into the ionosphere by the substorm, causing an intense westward electrojet in the midnight sector [*Kamide and Kokubun*, 1996]. The flag in SOPHIE means that we can eliminate times at which *SML* and *SMU* are of similar magnitudes and therefore eliminate times where an enhancement in ionospheric convection has been misidentified as a expansion phase onset [*Forsyth et al.*, 2015].

3. Methodology

In this paper, the polar projections of radial current density from AMPERE are used. We take current densities in a 90 min window encompassing substorm onset for the list of substorm onsets determined by SOPHIE [*Forsyth et al.*, 2015]. For each substorm onset, we refer to the magnetometer colatitude θ and MLT m given in the SuperMAG index data to determine the onset colatitude θ_0 and onset MLT m_0 of the substorm. We rotate the projection for each substorm by m_0, such that the data are transformed into a coordinate system defined

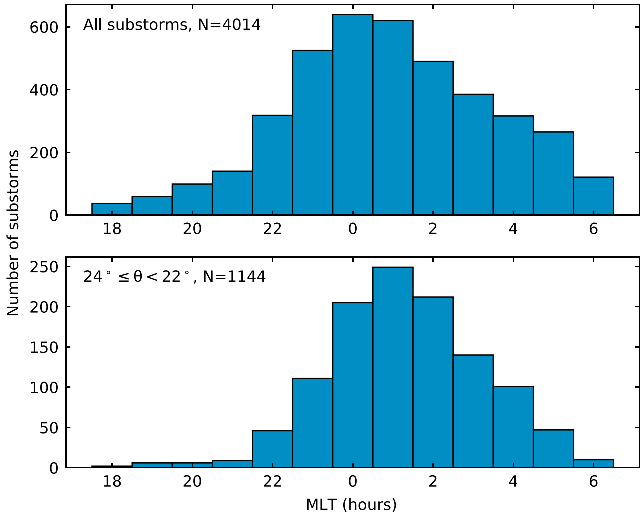

Figure 1. Histograms depicting the distribution of m_0 for the substorms contributing to (top) Figure 2 and for (bottom) Figure 4. We omit substorms for which the onset MLT was on the dayside ($6 < m_0 < 18$).

by substorm onset, in which $m'_0 = 0$ for each epoch. We discarded substorms for which $6 < m_0 < 18$, since they are on the dayside, and a histogram of the onset MLTs of the substorms which remained can be found in Figure 1.

We perform a superposed epoch analysis of the current densities in order to determine the behavior of the Birkeland currents through the epoch (Figure 2). We then filter our event list, only selecting substorms for which 22°< $\theta_0 \leq$ 24°, and then perform a superposed epoch analysis of this subset of the events (Figure 4).

The reason for transforming our coordinate system and analyzing a subset of the events is to reduce the amount of spatial variability in the results of our paper. By rotating each event by m_0, we ensure that any smoothing out of substorm features due to differences in the local time of substorm onset is minimized, and we more accurately reproduce the signatures as a result of the substorm. The same is true of taking a subset of the events defined by θ_0; by only taking events within a 2° range of onset colatitude, we reduce the smoothing of features due to the change in onset latitude and again more accurately reproduce the signatures as a result of the substorm. Previous studies of substorms with AMPERE have not done this [*Clausen et al.*, 2013b, 2013a] and consequently have been at risk of spatial smoothing.

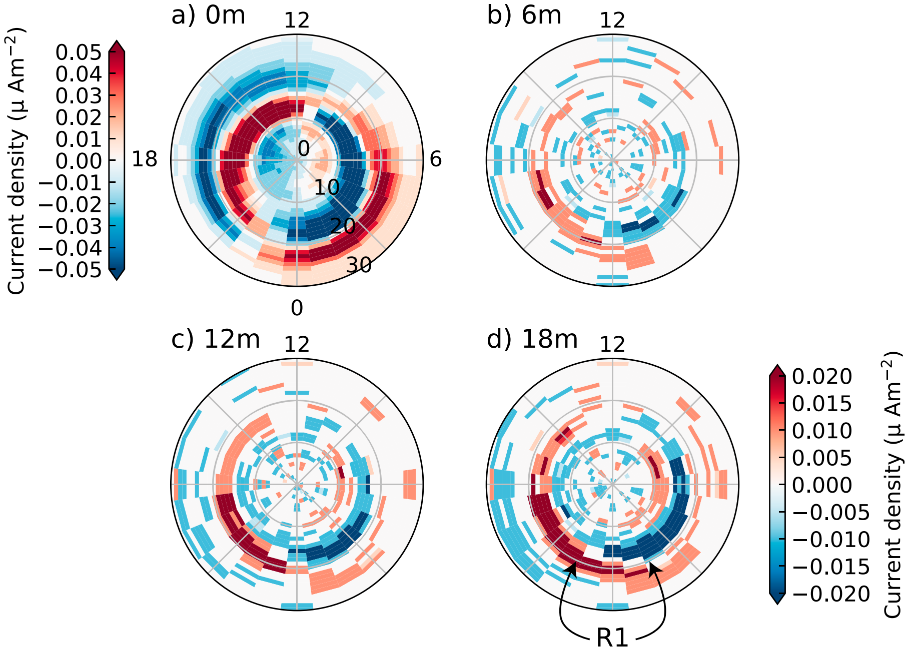

Figure 2. The median current densities for t = 0, 6, 12, and 18 min after substorm onset. Each panel is in polar coordinates, depicting the colatitudes 0–30° in the Northern Hemisphere for all hours of MLT. The color bar refers to (a) median current density $\bar{j_0}$ and the (b–d) difference in current density $\delta\bar{j}$. Substorms from all onset latitudes contribute to the median. The SCW is visible in R1 currents in Figures 2b–2d and is indicated in Figure 2d by black arrows. For a key to decipher which regions correspond to which features, see Figure 3. 4014 substorms contributed to these medians.

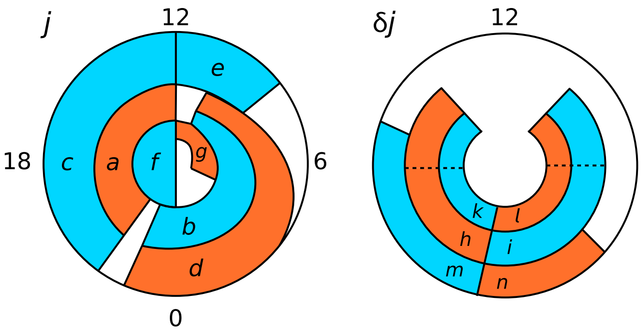

Figure 3. A key to decipher the regions of Figures 2 and 4 to which we refer in the text. (left) Regions found in plots of the median current density $\bar{j}_0$ (Figures 2a and 4a). (right) Regions found in plots of $\delta\bar{j}$ (Figures 2b–2d and 4b–4d). Dotted lines denote the poleward boundaries of regions h, i, k, and l as observed in Figures 2b–2d. Regions g, m, and n refer to features only in Figure 4. Regions do not correspond exactly to the features at hand, and this schematic is intended solely to guide the eye. Regions correspond to R1 current (a and b), R2 current (c–e), NBZ currents (f–g), enhanced R1 current (h and i), an expansion of the R1 current oval (k and l), and enhanced R2 current (m and n).

4. Reaction of the Birkeland Currents to Substorm Expansion Phase Onset

4.1. Median Morphology of the Birkeland Currents During Substorms

Figure 2 shows a superposed epoch analysis of 4014 substorms identified by SOPHIE. Figure 2a shows the polar projection of the median current density j at $t = 0$ m (henceforth $\bar{j}_0$), where t is the time since expansion phase onset determined from SOPHIE. We adopt the usual convention that upward current density is denoted by positive current density and downward current density is denoted by negative current density, and we use red to denote $j > 0$ μA m^{-2} and blue to denote $j < 0$ μA m^{-2}. Figures 2b–2d show $\bar{j}_0$ subtracted from the median current density before the polar projection is plotted, such that these panels show the difference in the current system between a given time t and $t = 0$ m, such that $\delta\bar{j} = \bar{j}_t - \bar{j}_0$. In these panels, red and blue refer to currents becoming more positive or more negative, rather than referring to the absolute value of current density. Figure 3 is drawn to aid the reader in identifying the region at hand; regions mentioned by letter in the text refer to Figure 3. As detailed in section 3, the current density corresponding to each substorm is rotated to the onset MLT of that substorm.

$\bar{j}_0$ (Figure 2a) shows the R1 and R2 current systems. The R1 current system is upward in the 12–22 MLT sector and downward in the 00–11 MLT sector (regions a and b). The R2 current system is downward in the 23–11 MLT sector and upward in the 11–21 MLT sector (regions c and d). The boundary between the two current systems at midnight is at a colatitude $\theta = 20°$, and the boundary at noon is at $\theta = 15°$, as a result of the polar cap being centered slightly toward the nightside. The poleward edge of the R1 current is at $\theta \sim 10°$, and the equatorward edge of the R2 current is at $\theta \sim 25°$.

At $\theta < 10°$, there is a region of downward j poleward of the R1 current system on the dusk flank within the polar cap (region f); this is the downward current of the NBZ current system. The NBZ current system is typically only found on the dayside of the polar cap but in this case extends onto the nightside. At $\theta > 25°$, the region of downward R2 current seems to wrap around to 09 MLT (region e). We do not expect dayside currents to be well ordered by the location of substorm onset, and as such, rotating the maps by m_0 as detailed in section 3 will cause currents being driven by dayside processes to be smeared out compared with an unrotated average; as such, region e and the nightside part of region f can be attributed to the smearing out of dayside-driven current systems by the rotation of the coordinate system to coordinates defined by a process occurring on the nightside of the Earth (section 3).

We now turn to Figures 2b–2d, in which we plot the evolution of the current system after substorm onset. On the nightside of Figure 2b ($t = 6$ m), there is a region of positive $\delta\bar{j}$ on the dusk flank (18–00 MLT) and a region of negative $\delta\bar{j}$ on the dawn flank (00–06 MLT) at $\theta > 15°$ (regions h and i, respectively). These regions intensify in Figures 2c and 2d ($t = 12$ m and 18 m). These regions (indicated by the arrows in Figure 2d) are consistent with either an additional or enhanced R1 current and are colocated with the equatorward edge of the R1 current systems. However, there is also a region of negative $\delta\bar{j}$ on the dusk flank (region k, bounded by the dotted line in Figure 3) and a region of positive $\delta\bar{j}$ on the dawn flank (region l, bounded by the dotted line in Figure 3) at $\theta < 15°$; these regions are colocated with the poleward edge of the R1 current.

4.2. Median Morphology During Substorms With Onset Colatitudes $22° < \theta_0 \leq 24°$

Previous studies [e.g., *Milan et al.*, 2007] have shown that substorms at lower latitudes tend to be larger. In Figure 4, we show similar results to Figure 2, but only for substorms with onset colatitudes $22° < \theta_0 \leq 24°$. Limiting the latitudinal range in this way reduces the number of events in the superposed epoch analysis

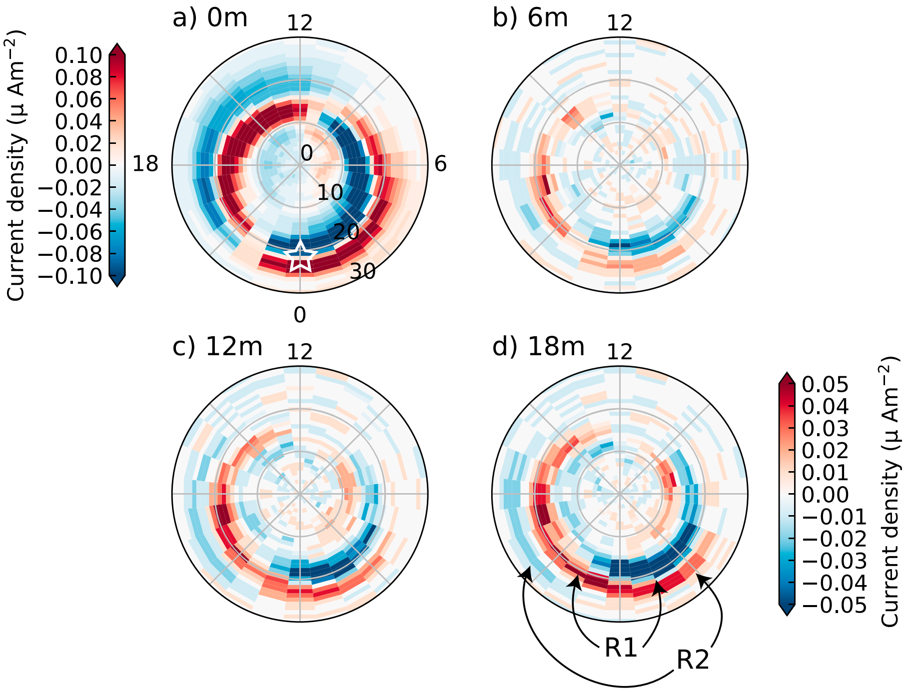

Figure 4. As in Figure 2, but only substorms at onset colatitudes $22° < \theta_0 \leq 24°$ contribute to the median. (a) A white star indicates the latitude of substorm onset to guide the eye, colocated with the latitude of the interface between R1 and R2 current. (b–d) The SCW is visible in both R1 and R2 currents and is indicated in Figure 4d by black arrows. For a key to decipher which regions correspond to which features, see Figure 3. 1144 substorms contributed to these medians.

to 1144 and also reduces the spatial variability in the events. The R1 and R2 current systems are present in Figure 4a in the same MLT sectors as Figure 2a but are stronger (Figure 3, regions a–e). In Figure 4a, the poleward edge of the R1 current is at $\theta \sim 15°$ at midnight and $\theta \sim 10°$ at noon, and the equatorward edge of the R2 current is at $\theta \sim 27°$ at midnight and $\theta \sim 24°$ at noon.

The interface between R1 and R2 in Figure 4a has moved equatorward, compared to the boundary seen in Figure 2a, to a colatitude $\theta = 23°$ at midnight; this is colocated with the onset latitudes of the substorms contributing to the plot and is illustrated by a white star overlaid in Figure 4a. This indicates that R1 current is flowing into the ionosphere poleward of the latitude of substorm onset, and R2 current is flowing out of the ionosphere equatorward of substorm onset. As in Figure 2a, the interface at noon is located 5° poleward, at $\theta = 17°$.

At $\theta < 10°$, there is a region of downward j poleward of R1 on the dusk flank (region f) and there is an additional region of upward j poleward of R1 on the dawn flank (region g). These signatures are again indicative of the presence of an NBZ current system at high latitudes, and the presence of a downward current and an upward current region can be explained by the lower spatial variability in Figure 4. The rotation of the current densities to the local time of substorm onset results in the signatures extending into the nightside of the polar cap.

As in Figures 2b–2d, subsequent to substorm onset, there is an enhancement in the R1 current seen in Figure 4b ($t = 6$ m), with this enhancement increasing in Figures 4c and 4d ($t = 12$ m and 18 m). Figure 4d shows two regions of $\delta\bar{j}$ at $22° > \theta > 15°$: a region of positive $\delta\bar{j}$ in the 12–21 MLT sector (region h) and a region of negative $\delta\bar{j}$ in the 23–09 MLT sector (region i). These regions (indicated by "R1" arrows in Figure 4d) are consistent with enhanced R1 current and are colocated with the equatorward boundary of the R1 current. At $15° > \theta > 10°$ there is a region of negative $\delta\bar{j}$ in the 12–21 MLT sector (region k) and a region of positive $\delta\bar{j}$ in the 23–09 MLT sector (region l); these regions are again consistent with R1 current oval expansion shortly after the substorm.

Additionally, at $30° > \theta > 22°$ in Figures 4b–4d, there is a region of downward $\delta\bar{j}$ in the 17–22 MLT sector (region m) and a region of upward $\delta\bar{j}$ in the 23–04 MLT sector (section n). These two regions

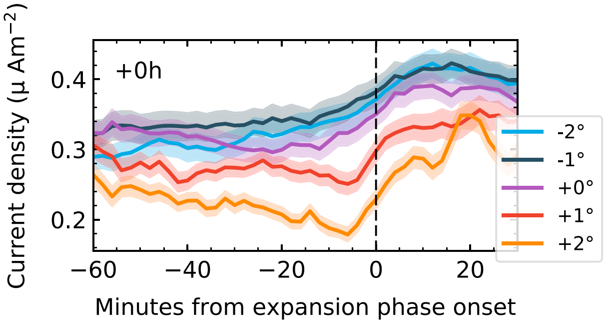

Figure 5. A plot of minutes since substorm onset t against mean current density j for the local time of substorm onset and the latitudes shown in the legend (relative to the latitude of substorm onset, such that positive latitudes are poleward of the onset latitude and negative latitudes are equatorward). The shaded area around each line is the standard error on the mean. Only events in which the coordinate contained upward current density (associated with downward precipitating electrons) are selected for averaging. The number of events contributing to each mean, from −2° to 2°, is 232, 221, 140, 63, and 31.

(indicated by arrows to "R2" in Figure 4d) are consistent with enhanced R2 currents and are colocated with the R2 current in Figure 4a. This enhancement of R2 current was not apparent in Figures 2b–2d, and we attribute this to the lower spatial variability of Figure 4 compared with Figure 2. We thus establish that we can see the substorm current wedge with AMPERE statistically and with enhancements in both R1 and R2 current in the case of Figure 4.

4.3. Upward Current Density Local to Substorm Onset

As shown in Figures 2 and 4, there is a global enhancement of the Birkeland currents after onset. Here we examine the behavior of the currents leading up to substorm onset in order to investigate whether the behavior of the currents is consistent with dimming of the aurora shortly before substorm onset [*Pellinen and Heikkila*, 1978; *Murphy et al.*, 2012].

In order to do that, we examine the current density at the MLT of substorm onset by plotting the mean current density against time for latitudes within ±2° from the onset latitude of the substorm (Figure 5). We select the mean rather than the median so that we can calculate the standard error, which is the shaded area plotted on either side of each line. We iterate through each combination of MLT and latitude, and we select all the substorms from our data set that had an upward current density for that combination throughout the epoch. We repeat this for every combination of MLT and latitude, such that different events may be contributing to the mean in each latitude plotted in Figure 5. The number of events contributing to each of the time series are given in the caption of the plot. This criterion is adopted to better examine the upward current density, associated with the downward precipitating electrons responsible for auroral emissions.

From $t = -20$ m until after substorm onset, the upward currents equatorward of the onset latitude rise. In contrast, the upward currents poleward of the onset latitude decrease. The mean upward current at both

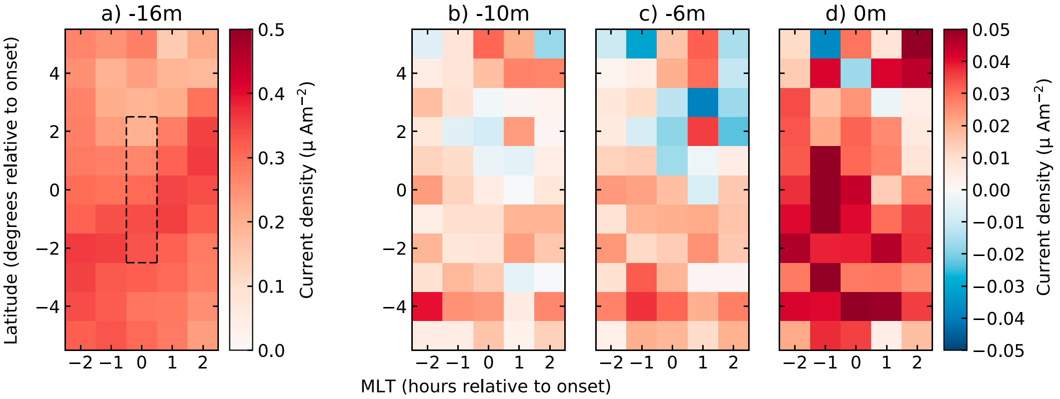

Figure 6. Maps of the mean current density against MLT and latitude relative to the location of substorm onset at different times t. (a) The average current density j in μA m^{-2} at $t = -16$ m. (b–d) The difference in current density from Figure 6a $\delta\bar{j}$, with substorm onset in Figure 6d. Only events in which the coordinate contained upward current density (associated with downward precipitating electrons) are selected for averaging. The reader should note that 1 h of MLT is equal to 15°, such that the x axis represents more distance than the y axis. The dashed box in Figure 6a shows the bins which are plotted in Figure 5. As in Figure 5, positive latitudes are poleward of the onset latitude and negative latitudes are equatorward. For the number of substorms contributing to each mean, see Figure 7.

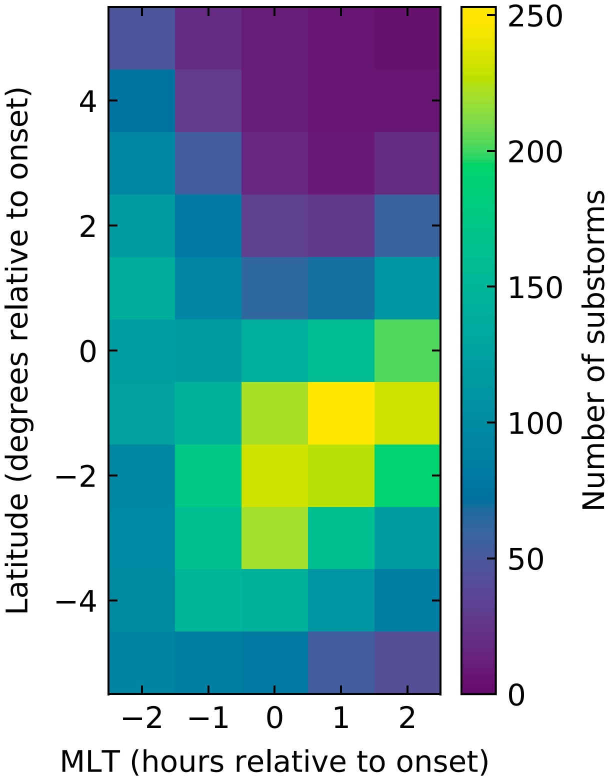

Figure 7. The same parameter space as shown in Figure 6, color coded by the number of substorms contributing to each bin.

relative latitudes +1° and +2° shows a drop during -30 m$< t < 5$ m for +2° and during -20 m$< t < 5$ m for +1°. The current densities begin to rise sharply at $t = -5$ m and carry on rising after the substorm onset.

Figure 6 shows a map of the mean change in current density close to the local time and colatitude of substorm onset (the number of events in each of the bins is plotted in Figure 7). Again, we iterate through each combination of MLT and latitude, selecting substorms for which the current density is upward at that combination throughout the epoch, such that different events might contribute to each bin. In this figure, the current density at $t = -16$ m is subtracted from each subsequent plot to find the change in current density until substorm onset. At $t = -10$ m, the current density increases across the parameter space, except for small decreases in the currents in the midnight local time sector. In the plot of $t = -6$ m the current density is generally reduced, up to 4° poleward of onset within 2 h of local time of onset; current density is generally increased equatorward of the latitude of onset. At $t = 0$ m, all current densities are substantially enhanced, indicating that any reduction only happens immediately prior to onset.

5. Discussion

5.1. Median Morphology of the Birkeland Currents

Do both the R1 and R2 current systems contribute to the substorm current wedge after substorm onset? A clear Region 1 current (regions a–b) and a clear R2 current system (regions c–e) are visible in the median current density at substorm onset (Figures 2a and 4a). Figures 2b–2d clearly show the R1 current system after substorm onset, as can be seen by examination of regions h and i. The expansion of the R1 current oval can also be seen in regions k and l, but there is no corresponding R2 current system (see regions m and n), seemingly supporting past results implying that the SCW is only seen in R1 currents [*Clausen et al.*, 2013b, 2013a].

In Figure 4, we analyze that a subset of the events by θ_0 reduces the spatial variability in latitude, and so the clearly observed R1 and R2 currents seen in Figures 4b–4d show that the lack of R2 current observed in Figure 2 is simply an effect of latitudinal averaging. The enhancement and the expansion of the R1 current oval (regions h–l) is present as it is in Figures 2b–2d, but there is also an enhancement of the R2 current oval (regions m and n), which is consistent with previous observations [*Murphy et al.*, 2013; *Chu et al.*, 2014; *Coxon et al.*, 2014b; *Sergeev et al.*, 2014b]. *Clausen et al.* [2013a] did not rotate the Birkeland currents to the MLT of the substorm onset and also did not bin them by the latitude of substorm onset, such that the spatial variability in their study was high; we conclude that by reducing the spatial variability, the signature of the SCW is clearer. Since there are regions of $\delta\bar{j}$ consistent with R1 and R2 current enhancement (regions h, i, m, and n), we conclude that both contribute to the SCW.

At onset, the current magnitudes increase quickly, with R1 current density increasing faster than R2 current density. This is consistent with observations of current magnitude made by *Coxon et al.* [2014b], who concluded that this was a signature of the substorm electrojet (from the schematic of *Clauer and McPherron* [1974]). R1 current flowing into the polar cap (region i) must flow out of the polar cap again, and this usually occurs via a Pedersen current flowing to a region of upward R2 current (from region i to region n). However, as the R1 current density shows larger enhancements than the R2 current density, this implies that some R1 current must flow west (toward dusk) and close through the upward R1 current on the other side of the polar cap (from region i to region h) [*Coxon et al.*, 2014b].

The existence of region 2 current in the SCW supports several models of the SCW which have suggested that this should be the case. In one model [*Birn et al.*, 1999; *Birn and Hesse*, 2014], R1 current is closed by the substorm electrojet in the ionosphere and by a current flowing across the magnetotail, but the R2 current is supplied by two closed loops on either side of the current disruption in the magnetotail, and the R2 current is smaller than the R1 current [*Kepko et al.*, 2015; after *Birn et al.*, 2011, *Birn et al.*, 2011]. Work suggesting that the SCW is composed of multiple "wedgelets," driven by bursty bulk flows, implies that azimuthal flow channels lead to shears which then lead to R1 and R2 currents [*Birn and Hesse*, 2013], but it should be noted that recent papers do not necessarily support a wedgelet-driven model of the SCW [*Forsyth et al.*, 2014b]. An alternative explanation for the R2 currents observed in the SCW is one in which both R1 and R2 are closed by the substorm electrojet in the ionosphere and currents flowing across the magnetotail [*Ritter and Lühr*, 2008; *Sergeev et al.*, 2011, 2014a]. The primary difference in these two models is to do with how the currents close in the magnetosphere, which we cannot investigate with the view of the ionospheric current systems afforded by AMPERE. Until the models make quantitative predictions on the ionospheric current flow during a substorm, we cannot differentiate between the two.

It is well known that the location of substorm onset varies in both local time and latitude [*Frey et al.*, 2004]. The extent of the substorm bulge varies from event to event, although is generally larger for substorms initiated at lower latitudes [*Milan et al.*, 2009]. Furthermore, the duration of each substorm expansion phase is variable. As such, creating maps of the average substorm currents using a superposed epoch will naturally average over these modes of variability. We note, for example, that the superposed epoch analysis results of the AMPERE data presented by *Clausen et al.* [2013a] show very little current in the 23–01 MLT sectors. In this study, we have removed two of these modes of variability by rotating the data into a coordinate system such that there is a common local time of substorm onset and by selecting those substorms whose onset occurs in a narrow colatitudinal range ($22^\circ < \theta_0 \leq 24^\circ$). As a result of this, our results show the Region 1 and Region 2 currents extending across the whole of the nightside, which is in contrast to the results of *Clausen et al.* [2013a].

However, the remaining sources of variability will still cause smoothing out in terms of the change in the median current density through the substorm. Our observed change in median current density $\delta\bar{j}$ is of a magnitude consistent with previous studies [*Clausen et al.*, 2013b, 2013a], but the median current density $\delta\bar{j}_0$ is equal to no more than 0.2 μA m^{-2} in Figures 2a and 4a, whereas most observations of Birkeland currents show them to be in the range $0.15 \leq j \leq 1.0$ μA m^{-2} [e.g., *Clausen et al.*, 2012, Figure 2]. We interpret the fact that $\bar{j}_0$ is lower in Figure 2a than in Figure 4a as an indication that increased averaging over colatitude leads to a reduction in the median and we therefore infer that our medians are lower than expected due to the remaining sources of variability in the substorm.

The identification of substorm onsets will also, naturally, influence the results of the superposed epoch analysis study. Here we use the expansion phase onsets immediately preceded by an interval of no substorm activity from the SOPHIE technique [*Forsyth et al.*, 2015]. This technique identifies substorm expansion, recovery phases using the SuperMAG *AL* (*SML*) index, which is generated from over 100 magnetometer stations distributed throughout the auroral region [*Newell and Gjerloev*, 2011]. *Forsyth et al.* [2015] showed that the substorm onset times identified by this technique were closely aligned with those from orbiting imagers. In this study, the onset location is defined as the location of the magnetometer station providing the *SML* index at the time of substorm onset. While there is some uncertainty in the location of onset due to the spatial coverage of the magnetometers contributing to the SuperMAG data set, we do a good job of identifying the onset from ground magnetometers given the lack of a reliable onset list based on auroral data.

A region of NBZ current (region f in Figure 2a and regions f and g in Figure 4a) is within the polar cap, at high latitudes ($\theta < 10°$). The observation of NBZ current on the dayside is consistent with previous observations of NBZ currents within the polar cap on the dayside [*Iijima et al.*, 1984; *Zanetti et al.*, 1984; *Weimer*, 2001]. The observed NBZ currents in Figures 2a and 4a indicate that there are substorms for which IMF is northward at the point of substorm onset. Northward turnings of the IMF are often coincident with substorm onset, despite not being required to trigger substorm onset [*Freeman and Morley*, 2009]. Superposed epoch analyses of dayside reconnection rate Φ_D also show that the dayside reconnection rate peaks when $t < 0$ m [*Coxon et al.*, 2014b], which is consistent with less southward IMF at $t = 0$ m. The statistical locations of the NBZ currents found in *Weimer* [2001] confirm that these currents are of the appropriate sense for the NBZ current system and also confirms that the downward NBZ current density dominates the upward current density, which explains why higher spatial variability in Figure 2 obscures this signature. We do not interpret this signature as a region 0 (R0) current associated with the SCW, because previous observations and modeling of R0 current during substorms have found R0 to be very narrow and only just poleward of the R1 current sheet. The region identified as NBZ is thicker and farther poleward than the R0 currents previously observed during substorms [*Fujii et al.*, 1994; *Hoffman et al.*, 1994; *Gjerloev and Hoffman*, 2002].

In Figures 2b–2d and 4b–4d, regions k and l indicate that the R1 current at the poleward edge is decreasing, consistent with an expansion of the current ovals to lower latitudes leading to less current flowing at high latitudes. Although the expanding/contracting polar cap paradigm [*Cowley and Lockwood*, 1992] indicates that the onset of nightside reconnection should lead to a contraction of the polar cap (and therefore the current ovals), observations of the average colatitude of the Birkeland current ovals during substorms have shown that this contraction does not begin until $t \sim 20$ m [*Coxon et al.*, 2014b]. Since all the plots presented show times before this point, the current ovals will be expanding in each plot, consistent with the observations herein. Two caveats should be noted regarding this point, however. First, auroral images have shown that the auroral oval at local times near midnight contracts nearly instantaneously after the onset of a substorm, which may indicate that the oval is not expanding at nightside MLTs [*Gjerloev et al.*, 2007] despite previous studies showing an increase in average colatitude after onset [*Coxon et al.*, 2014b]. Second, these observations are also consistent with observations of narrow R0 current sheets playing a part in the SCW, flowing poleward of R1 current and in the opposite direction to R1 current. *Gjerloev and Hoffman* [2002] proposed a model in which R0 current flows poleward of R1 current on both sides of midnight, and previous observations have also shown R0 current flowing during substorms [*Fujii et al.*, 1994; *Hoffman et al.*, 1994]. As such, while the observations herein are consistent with an expansion such as the one reported by *Coxon et al.* [2014b], they are also consistent with the model of *Gjerloev and Hoffman* [2002].

In Figure 4, the interface between the R1 and R2 current systems is located at $\theta = 23°$ at midnight, and the onset latitudes of the events plotted in this figure are $22° < \theta_0 \leq 24°$. We interpret this as evidence that the onset latitude of the substorm and the latitude of the interface between current systems are related. Previous observations of substorm onsets show that substorm onset typically occurs close to the Harang discontinuity [*Lyons et al.*, 2003, 2005; *Weygand et al.*, 2008; *Zou et al.*, 2009, 2013], which is associated with the interface between R1 and R2 current [*Iijima and Potemra*, 1978]. This implies that the latitude of the interface between R1 and R2 current should be the latitude of substorm onset, which is consistent with R1 currents colocated with the open/closed field line boundary [*Cowley*, 2000; *Clausen et al.*, 2013a] and R2 currents mapping to the partial ring current [*Iijima and Potemra*, 1978]. The implication is also consistent with the two-loop SCW model, which predicts R1 and R2 current flowing from the current disruption in the tail to the ionosphere [*Sergeev et al.*, 2011, 2014a]; this result implies that the R1 current flows from the ionosphere and some region tailward of the current disruption, and R2 current flows from the ionosphere to some region earthward of the current disruption.

5.2. Upward Current Density Local to Substorm Onset

In three case studies, *Murphy et al.* [2012] examined the current density from AMPERE at the local time of onset, in a range of 6° close to the latitude of substorm onset, and found evidence for a reduction in Birkeland current densities immediately prior to substorm onset. The authors interpreted this for evidence of auroral dimming after the result of *Pellinen and Heikkila* [1978]. In order to determine the existence of this reduction in Birkeland current statistically, we examine the upward current density at latitudes close to substorm onset (Figures 5 and 6).

Interestingly, we do indeed observe a reduction in Birkeland current density prior to substorm onset 1 – 2° poleward of the substorm. However, we find no evidence for a similar reduction at or equatorward of the latitude of the substorm. The observed decrease in current density is very localized, but despite this, we interpret it as a reduction in current rather than a movement of current, since we do not observe a commensurate increase in current density equatorward of the substorm latitude. Our observations are consistent with the result of *Murphy et al.* [2012], who also observed a reduction in current density poleward of the substorm onset latitude, and also consistent with the result of *Pellinen and Heikkila* [1978], who reported Airborne Ionospheric Laboratory observations showing a quiet arc fading and then reappearing 1 – 2 m before an arc to the south developed into a major auroral breakup (marking substorm onset).

We specifically examine the upward current density because it is that which is associated with the downward precipitating electrons associated with auroral emissions. Despite the fact that the electrons which carry Birkeland current may not be responsible for auroral emission, studies have shown that current and aurora are generally colocated [*Armstrong et al.*, 1975; *Kamide and Akasofu*, 1976]. More recently, work by *Murphy et al.* [2012] showed that discrete auroral forms were colocated with regions of upward Birkeland current, and *Carter et al.* [2016] compared AMPERE data to IMAGE data by parameterizing both data sets using solar wind data, in order to evaluate the correspondence between auroral emission and Birkeland current. They found a good correspondence between upward current density and auroral emission at all local times, which further bolsters the assumption made here.

We cautiously interpret the reductions in Figures 5 and 6 as evidence for auroral dimming, but it must be stressed that these results are at the very limit of AMPERE's ability to resolve the current systems, both spatially and temporally. Because we select only intervals that are all upward current, the number of events in each mean is lower than the number in the averages presented and discussed in sections 4.1 and 5.1 by an order of magnitude, and the decrease is only just beyond the margin of error. With these caveats in mind, we interpret the result as evidence for auroral dimming in observations of upward Birkeland currents in support of *Murphy et al.* [2012]. We leave further studies of this phenomenon using higher-resolution and higher-cadence instrumentation as work for the future.

6. Conclusion

In this paper, we use AMPERE to address apparent disparities between previous studies of the structure of the substorm current wedge. In order to do this, we rotate current maps provided by AMPERE [*Anderson et al.*, 2000; *Waters et al.*, 2001] to the MLT of substorm expansion phase onset provided by SuperMAG [*Gjerloev*, 2012] and SOPHIE [*Forsyth et al.*, 2015], before binning the substorms by the latitude of substorm onset. By doing this, we demonstrate that both R1 and R2 current densities on the nightside increase subsequent to substorm onset, consistent with the two-loop substorm model [*Sergeev et al.*, 2011, 2014a] and supporting results [*Coxon et al.*, 2014b; *Sergeev et al.*, 2014b].

Additionally, we explore the morphology of the currents at and after substorm onset. We observe NBZ currents [*Iijima et al.*, 1984] at the point of substorm onset and attribute this signature to a northward turning of the IMF on average at substorm onset [*Freeman and Morley*, 2009]. We also find that the latitude of the boundary between the R1 and R2 current systems on the nightside of the polar cap in the polar projection of the median current density is coincident with the latitudes of the substorms contributing to the median. We link this to studies relating the Harang discontinuity to substorm onset [e.g., *Zou et al.*, 2013]. Modern models of the SCW predict an R2 component to the SCW but disagree on how this current closes in the magnetotail [e.g., *Birn and Hesse*, 2014; *Sergeev et al.*, 2014a]. Either more experimental work is needed to measure the signature of the SCW within the magnetotail or more concrete predictions of ionospheric signatures are needed for these models to be tested using AMPERE data.

Finally, we examine statistical evidence for auroral dimming [*Pellinen and Heikkila*, 1978; *Murphy et al.*, 2012] and we find evidence which suggests that the upward field-aligned current density is reduced between 15 and 5 min before onset, consistent with the timescales of the previous auroral observations

[*Pellinen and Heikkila*, 1978]. The phenomenon appears to be very localized, which is also consistent with previous attempts to link auroral dimming to current density [*Murphy et al.*, 2012]. Further work, with instrumentation of higher resolution and cadence, is needed to fully quantify this phenomenon.

Acknowledgments
This work was supported by NERC joint grants NE/L007177/1 (J.C.C. and C.M.J.) and NE/L007495/1 (I.J.R. and C.F.), in addition to STFC Ernest Rutherford grant ST/L002809/1 (J.C.C. and R.C.F.). AMPERE data used were downloaded from http://ampere.jhuapl.edu/, and SuperMAG data used were downloaded from http://supermag.jhuapl.edu/; the SOPHIE data were taken from the supplementary material of *Forsyth et al.* [2015]. For the ground magnetometer data we gratefully acknowledge the following: Intermagnet; USGS, Jeffrey J. Love; CARISMA, PI Ian Mann; CANMOS; the S-RAMP database, PI K. Yumoto and K. Shiokawa; the SPIDR database; AARI, PI Oleg Troshichev; the MACCS program, PI M. Engebretson, Geomagnetism Unit of the Geological Survey of Canada; GIMA; MEASURE, UCLA IGPP and Florida Institute of Technology; SAMBA, PI Eftyhia Zesta; 210 Chain, PI K. Yumoto; SAMNET, PI Farideh Honary; the institutes who maintain the IMAGE magnetometer array, PI Eija Tanskanen; PENGUIN; AUTUMN, PI Martin Connors; DTU Space, PI Juergen Matzka; South Pole and McMurdo Magnetometer, PIs Louis J. Lanzarotti and Alan T. Weatherwax; ICESTAR; RAPIDMAG; PENGUIn; British Artarctic Survey; McMac, PI Peter Chi; BGS, PI Susan Macmillan; Pushkov Institute of Terrestrial Magnetism, Ionosphere and Radio Wave Propagation (IZMIRAN); GFZ, PI Juergen Matzka; MFGI, PI B. Heilig; IGFPAS, PI J. Reda; University of L'Aquila, PI M. Vellante; and SuperMAG, PI Jesper W. Gjerloev. Data analysis and plotting were conducted in Python. Specifically, the libraries used were NumPy, SciPy [*van der Walt et al.*, 2011], Matplotlib [*Hunter*, 2007], Pandas [*McKinney*, 2010], and SpacePy [*Morley et al.*, 2010].

References

Akasofu, S.-I. (1964), The development of the auroral substorm, *Planet. Space Sci.*, *12*(4), 273–282, doi:10.1016/0032-0633(64)90151-5.

Anderson, B. J., K. Takahashi, and B. A. Toth (2000), Sensing global Birkeland currents with Iridium® engineering magnetometer data, *Geophys. Res. Lett.*, *27*(24), 4045–4048, doi:10.1029/2000GL000094.

Anderson, B. J., H. Korth, C. L. Waters, D. L. Green, V. G. Merkin, R. J. Barnes, and L. P. Dyrud (2014), Development of large-scale Birkeland currents determined from the Active Magnetosphere and Planetary Electrodynamics Response Experiment, *Geophys. Res. Lett.*, *41*, 3017–3025, doi:10.1002/2014GL059941.

Armstrong, J. C., S. I. Akasofu, and G. Rostoker (1975), A comparison of satellite observations of Birkeland currents with ground observations of visible aurora and ionospheric currents, *J. Geophys. Res.*, *80*(4), 575–586, doi:10.1029/JA080i004p00575.

Birkeland, K. (1908), *The Norwegian Aurora Polaris Expedition 1902–1903*, vol. 1, H. Aschelhoug and Co., Christiania, Norway.

Birkeland, K. (1913), *The Norwegian Aurora Polaris Expedition 1902–1903*, vol. 2, H. Aschelhoug & Co., Christiania, Norway.

Birn, J., and M. Hesse (2013), The substorm current wedge in MHD simulations, *J. Geophys. Res. Space Physics*, *118*, 3364–3376, doi:10.1002/jgra.50187.

Birn, J., and M. Hesse (2014), The substorm current wedge: Further insights from MHD simulations, *J. Geophys. Res. Space Physics*, *119*, 3503–3513, doi:10.1002/2014JA019863.

Birn, J., M. Hesse, G. Haerendel, W. Baumjohann, and K. Shiokawa (1999), Flow braking and the substorm current wedge, *J. Geophys. Res.*, *104*(A9), 19,895–19,903, doi:10.1029/1999JA900173.

Birn, J., R. Nakamura, E. V. Panov, and M. Hesse (2011), Bursty bulk flows and dipolarization in MHD simulations of magnetotail reconnection, *J. Geophys. Res.*, *116*, A01210, doi:10.1029/2010JA016083.

Boström, R. (1964), A model of the auroral electrojets, *J. Geophys. Res.*, *69*(23), 4983–4999, doi:10.1029/JZ069i023p04983.

Boström, R. (1966), Auroral electric fields, 1–18, Dept. of Plasma Physics Report, KTH Royal Institute of Technology, Stockholm, Sweden. [Available at http://kth.diva-portal.org/smash/get/diva2:514489/FULLTEXT01.pdf.]

Carter, J. A., S. E. Milan, J. C. Coxon, M.-T. Walach, and B. J. Anderson (2016), Average field-aligned current configuration parameterized by solar wind conditions, *J. Geophys. Res. Space Physics*, *121*, 1294–1307, doi:10.1002/2015JA021567.

Chu, X., et al. (2014), Development and validation of inversion technique for substorm current wedge using ground magnetic field data, *J. Geophys. Res. Space Physics*, *119*, 1909–1924, doi:10.1002/2013JA019185.

Clauer, C. R., and R. L. McPherron (1974), Mapping the local time-universal time development of magnetospheric substorms using mid-latitude magnetic observations, *J. Geophys. Res.*, *79*(19), 2811–2820, doi:10.1029/JA079i019p02811.

Clausen, L. B. N., J. B. H. Baker, J. M. Ruohoniemi, S. E. Milan, and B. J. Anderson (2012), Dynamics of the region 1 Birkeland current oval derived from the Active Magnetosphere and Planetary Electrodynamics Response Experiment (AMPERE), *J. Geophys. Res.*, *117*, A06233, doi:10.1029/2012JA017666.

Clausen, L. B. N., J. B. H. Baker, J. M. Ruohoniemi, S. E. Milan, J. C. Coxon, S. Wing, S. Ohtani, and B. J. Anderson (2013a), Temporal and spatial dynamics of the regions 1 and 2 Birkeland currents during substorms, *J. Geophys. Res. Space Physics*, *118*, 3007–3016, doi:10.1002/jgra.50288.

Clausen, L. B. N., S. E. Milan, J. B. H. Baker, J. M. Ruohoniemi, K.-H. Glassmeier, J. C. Coxon, and B. J. Anderson (2013b), On the influence of open magnetic flux on substorm intensity: Ground- and space-based observations, *J. Geophys. Res. Space Physics*, *118*, 2958–2969, doi:10.1002/jgra.50308.

Cowley, S. W. H. (2000), Magnetosphere-ionosphere interactions: A tutorial review, in *Magnetospheric Current Systems, Geophys. Monogr. Ser.*, vol. 118, edited by S.-I. Ohtani et al., pp. 91–106, AGU, Washington, D. C.

Cowley, S. W. H., and M. Lockwood (1992), Excitation and decay of solar wind-driven flows in the magnetosphere-ionosphere system, *Ann. Geophys.*, *10*, 103–115.

Coxon, J. C., S. E. Milan, L. B. N. Clausen, B. J. Anderson, and H. Korth (2014a), The magnitudes of the regions 1 and 2 Birkeland currents observed by AMPERE and their role in solar wind-magnetosphere-ionosphere coupling, *J. Geophys. Res. Space Physics*, *119*, 9804–9815, doi:10.1002/2014JA020138.

Coxon, J. C., S. E. Milan, L. B. N. Clausen, B. J. Anderson, and H. Korth (2014b), A superposed epoch analysis of the regions 1 and 2 Birkeland currents observed by AMPERE during substorms, *J. Geophys. Res. Space Physics*, *119*, 9834–9846, doi:10.1002/2014JA020500.

Coxon, J. C., S. E. Milan, J. A. Carter, L. B. N. Clausen, B. J. Anderson, and H. Korth (2016), Seasonal and diurnal variations in AMPERE observations of the Birkeland currents compared to modeled results, *J. Geophys. Res. Space Physics*, *121*, 4027–4040, doi:10.1002/2015JA022050.

Coxon, J. C., S. E. Milan, and B. J. Anderson (2017), A review of Birkeland current research using AMPERE, in *Electric Currents: Geospace and Beyond, Geophys. Monogr. Ser.*, edited by A. Keiling, O. Marghitu, and M. Wheatland, AGU, Washington, D. C.

Cummings, W. D., and A. J. Dessler (1967), Field-aligned currents in the magnetosphere, *J. Geophys. Res.*, *72*(3), 1007–1013, doi:10.1029/JZ072i003p01007.

Davis, T. N., and M. Sugiura (1966), Auroral electrojet activity index AE and its universal time variations, *J. Geophys. Res.*, *71*(3), 785–801, doi:10.1029/JZ071i003p00785.

Dungey, J. W. (1961), Interplanetary magnetic field and the auroral zones, *Phys. Rev. Lett.*, *6*, 47–48.

Forsyth, C., et al. (2014a), In situ spatiotemporal measurements of the detailed azimuthal substructure of the substorm current wedge, *J. Geophys. Res. Space Physics*, *119*, 927–946, doi:10.1002/2013JA019302.

Forsyth, C., et al. (2014b), Increases in plasma sheet temperature with solar wind driving during substorm growth phases, *Geophys. Res. Lett.*, *41*, 8713–8721, doi:10.1002/2014GL062400.

Forsyth, C., I. J. Rae, J. C. Coxon, M. P. Freeman, C. M. Jackman, J. Gjerloev, and A. N. Fazakerley (2015), A new technique for determining Substorm Onsets and Phases From Indices of the Electrojet (SOPHIE), *J. Geophys. Res. Space Physics*, *120*, 10,592–10,606, doi:10.1002/2015JA021343.

Freeman, M. P., and S. K. Morley (2009), No evidence for externally triggered substorms based on superposed epoch analysis of IMF B_z, *Geophys. Res. Lett.*, *36*, L21101, doi:10.1029/2009GL040621.

Frey, H. U., S. B. Mende, V. Angelopoulos, and E. F. Donovan (2004), Substorm onset observations by IMAGE-FUV, *J. Geophys. Res.*, *109*, A10304, doi:10.1029/2004JA010607.

Fujii, R., and T. Iijima (1987), Control of the ionospheric conductivities on large-scale Birkeland current intensities under geomagnetic quiet conditions, *J. Geophys. Res.*, *92*(A5), 4505–4513, doi:10.1029/JA092iA05p04505.

Fujii, R., R. A. Hoffman, P. C. Anderson, J. D. Craven, M. Sugiura, L. A. Frank, and N. C. Maynard (1994), Electrodynamic parameters in the nighttime sector during auroral substorms, *J. Geophys. Res.*, *99*(A4), 6093–6112, doi:10.1029/93JA02210.

Gjerloev, J. W. (2012), The SuperMAG data processing technique, *J. Geophys. Res.*, *117*, A09213, doi:10.1029/2012JA017683.

Gjerloev, J. W., and R. A. Hoffman (2002), Currents in auroral substorms, *J. Geophys. Res.*, *107*(A8), 1163, doi:10.1029/2001JA000194.

Gjerloev, J. W., R. A. Hoffman, J. B. Sigwarth, and L. A. Frank (2007), Statistical description of the bulge-type auroral substorm in the far ultraviolet, *J. Geophys. Res.*, *112*, A07213, doi:10.1029/2006JA012189.

Hoffman, R. A., R. Fujii, and M. Sugiura (1994), Characteristics of the field-aligned current system in the nighttime sector during auroral substorms, *J. Geophys. Res.*, *99*(A11), 21,303–21,325, doi:10.1029/94JA01659.

Hunter, J. D. (2007), Matplotlib: A 2D graphics environment, *Comput. Sci. Eng.*, *9*(3), 90–95, doi:10.1109/MCSE.2007.55.

Iijima, T., and T. A. Potemra (1976), The amplitude distribution of field-aligned currents at northern high latitudes observed by Triad, *J. Geophys. Res.*, *81*, 2165–2174.

Iijima, T., and T. A. Potemra (1978), Large-scale characteristics of field-aligned currents associated with substorms, *J. Geophys. Res.*, *83*, 599–615.

Iijima, T., T. A. Potemra, L. J. Zanetti, and P. F. Bythrow (1984), Large-scale Birkeland currents in the dayside polar region during strongly northward IMF: A new Birkeland current system, *J. Geophys. Res.*, *89*(A9), 7441–7452, doi:10.1029/JA089iA09p07441.

Kamide, Y., and S. I. Akasofu (1976), The location of the field-aligned currents with respect to discrete auroral arcs, *J. Geophys. Res.*, *81*(22), 3999–4003, doi:10.1029/JA081i022p03999.

Kamide, Y., and S. Kokubun (1996), Two-component auroral electrojet: Importance for substorm studies, *J. Geophys. Res.*, *101*(A6), 13,027–13,046, doi:10.1029/96JA00142.

Kepko, L., R. L. McPherron, O. Amm, S. Apatenkov, W. Baumjohann, J. Birn, M. Lester, R. Nakamura, T. I. Pulkkinen, and V. Sergeev (2015), Substorm current wedge revisited, *Space Sci. Rev.*, *190*(1), 1–46, doi:10.1007/s11214-014-0124-9.

Lockwood, M., and S. W. H. Cowley (1992), Ionospheric convection and the substorm cycle, in *Substorms. 1: Proceedings of the First International Conference on Substorms*, vol. 1, pp. 99–109, European Space Agency, Kiruna, Sweden.

Lyons, L. R., C.-P. Wang, and T. Nagai (2003), Substorm onset by plasma sheet divergence, *J. Geophys. Res.*, *108*(A12), 1427, doi:10.1029/2003JA010178.

Lyons, L. R., D.-Y. Lee, C.-P. Wang, and S. B. Mende (2005), Global auroral responses to abrupt solar wind changes: Dynamic pressure, substorm, and null events, *J. Geophys. Res.*, *110*, A08208, doi:10.1029/2005JA011089.

McKinney, W. (2010), Data structures for statistical computing in Python, in *Proceedings of the 9th Python in Science Conference*, edited by S. van der Walt and J. Millman, pp. 51–56.

McPherron, R. L. (1970), Growth phase of magnetospheric substorms, *J. Geophys. Res.*, *75*(28), 5592–5599, doi:10.1029/JA075i028p05592.

Milan, S. E., G. Provan, and B. Hubert (2007), Magnetic flux transport in the Dungey cycle: A survey of dayside and nightside reconnection rates, *J. Geophys. Res.*, *112*, A01209, doi:10.1029/2006JA011642.

Milan, S. E., A. Grocott, C. Forsyth, S. M. Imber, P. D. Boakes, and B. Hubert (2009), A superposed epoch analysis of auroral evolution during substorm growth, onset and recovery: Open magnetic flux control of substorm intensity, *Ann. Geophys.*, *27*(2), 659–668, doi:10.5194/angeo-27-659-2009.

Milan, S. E., J. A. Carter, H. Korth, and B. J. Anderson (2015), Principal component analysis of Birkeland currents determined by the Active Magnetosphere and Planetary Electrodynamics Response Experiment, *J. Geophys. Res. Space Physics*, *120*, 10,415–10,424, doi:10.1002/2015JA021680.

Morley, S. K., J. Koller, D. T. Welling, B. A. Larsen, M. G. Henderson, and J. T. Niehof (2010), SpacePy—A Python-based library of tools for the space sciences, in *Proceedings of the 9th Python in Science Conference (SciPy 2010)*, edited by S. van der Walt and J. Millman, pp. 39–45, Austin, Tex.

Murphy, K. R., I. R. Mann, I. J. Rae, C. L. Waters, B. J. Anderson, D. K. Milling, H. J. Singer, and H. Korth (2012), Reduction in field-aligned currents preceding and local to auroral substorm onset, *Geophys. Res. Lett.*, *39*, L15106, doi:10.1029/2012GL052798.

Murphy, K. R., I. R. Man, I. Jonathan Rae, C. L. Waters, H. U. Frey, A. Kale, H. J. Singer, B. J. Anderson, and H. Korth (2013), The detailed spatial structure of field-aligned currents comprising the substorm current wedge, *J. Geophys. Res. Space Physics*, *118*, 7714–7727, doi:10.1002/2013JA018979.

Newell, P. T., and J. W. Gjerloev (2011), Evaluation of SuperMAG auroral electrojet indices as indicators of substorms and auroral power, *J. Geophys. Res.*, *116*, A12211, doi:10.1029/2011JA016779.

Pellinen, R. J., and W. J. Heikkila (1978), Observations of auroral fading before breakup, *J. Geophys. Res.*, *83*(A9), 4207–4217, doi:10.1029/JA083iA09p04207.

Ritter, P., and H. Lühr (2008), Near-earth magnetic signature of magnetospheric substorms and an improved substorm current model, *Ann. Geophys.*, *26*(9), 2781–2793, doi:10.5194/angeo-26-2781-2008.

Sergeev, V. A., N. A. Tsyganenko, M. V. Smirnov, A. V. Nikolaev, H. J. Singer, and W. Baumjohann (2011), Magnetic effects of the substorm current wedge in a “spread-out wire” model and their comparison with ground, geosynchronous, and tail lobe data, *J. Geophys. Res.*, *116*, A07218, doi:10.1029/2011JA016471.

Sergeev, V. A., A. V. Nikolaev, N. A. Tsyganenko, V. Angelopoulos, A. V. Runov, H. J. Singer, and J. Yang (2014a), Testing a two-loop pattern of the Substorm Current Wedge (SCW2L), *J. Geophys. Res. Space Physics*, *119*, 947–963, doi:10.1002/2013JA019629.

Sergeev, V. A., et al. (2014b), Event study combining magnetospheric and ionospheric perspectives of the substorm current wedge modeling, *J. Geophys. Res. Space Physics*, *119*, 9714–9728, doi:10.1002/2014JA020522.

Shore, R. M., M. P. Freeman, J. A. Wild, and J. W. Gjerloev (2017), A high-resolution model of the external and induced magnetic field at the Earth’s surface in the Northern Hemisphere, *J. Geophys. Res. Space Physics*, *122*, 2440–2454, doi:10.1002/2016JA023682.

Siscoe, G. L., and T. S. Huang (1985), Polar cap inflation and deflation, *J. Geophys. Res.*, *90*(A1), 543–547, doi:10.1029/JA090iA01p00543.

van der Walt, S., S. C. Colbert, and G. Varoquaux (2011), The NumPy array: A structure for efficient numerical computation, *Comput. Sci. Eng.*, *13*(2), 22–30, doi:10.1109/MCSE.2011.37.

Waters, C. L., B. J. Anderson, and K. Liou (2001), Estimation of global field-aligned currents using the Iridium® System magnetometer data, *Geophys. Res. Lett.*, *28*(11), 2165–2168, doi:10.1029/2000GL012725.

Weimer, D. R. (2001), Maps of ionospheric field-aligned currents as a function of the interplanetary magnetic field derived from Dynamics Explorer 2 data, *J. Geophys. Res.*, *106*(A7), 12,889–12,902, doi:10.1029/2000JA000295.

Weygand, J. M., R. L. McPherron, H. U. Frey, O. Amm, K. Kauristie, A. Viljanen, and A. Koistinen (2008), Relation of substorm onset to Harang discontinuity, *J. Geophys. Res.*, *113*, A04213, doi:10.1029/2007JA012537.

Zanetti, L. J., T. A. Potemra, T. Iijima, W. Baumjohann, and P. F. Bythrow (1984), Ionospheric and Birkeland current distributions for northward interplanetary magnetic field: Inferred polar convection, *J. Geophys. Res.*, *89*(A9), 7453–7458, doi:10.1029/JA089iA09p07453.

Zmuda, A. J., J. H. Martin, and F. T. Heuring (1966), Transverse magnetic disturbances at 1100 kilometers in the auroral region, *J. Geophys. Res.*, *71*, 5033–5045.

Zou, S., L. R. Lyons, C.-P. Wang, A. Boudouridis, J. M. Ruohoniemi, P. C. Anderson, P. L. Dyson, and J. C. Devlin (2009), On the coupling between the Harang reversal evolution and substorm dynamics: A synthesis of SuperDARN, DMSP, and IMAGE observations, *J. Geophys. Res.*, *114*, A01205, doi:10.1029/2008JA013449.

Zou, S., L. R. Lyons, and Y. Nishimura (2013), Mutual evolution of aurora and ionospheric electrodynamic features near the Harang reversal during substorms, in *Auroral Phenomenology and Magnetospheric Processes: Earth And Other Planets*, edited by A. Keiling et al., pp. 159–170, AGU, Washington, D. C., doi:10.1029/2011GM001163.